Optics Letters

Logistic splicing correction for VNIR–SWIR reflectance imaging spectroscopy

Federico Grillini,[1,*] Jean-Baptiste Thomas,[1,2] and Sony George[1]

[1]Colourlab, Norwegian University of Science and Technology (NTNU), Norway
[2]ImViA Laboratory, University of Burgundy, France
*Corresponding author: federico.grillini@ntnu.no

Received 20 October 2022; revised 8 December 2022; accepted 12 December 2022; posted 12 December 2022; published 5 January 2023

In the field of spectroscopy, a splicing correction is a process by which two spectra captured with different sensors in adjacent or overlapping electromagnetic spectrum ranges are smoothly connected. In our study, we extend this concept to the case of reflectance imaging spectroscopy in the visible–near-infrared (VNIR) and short-wave infrared (SWIR), accounting for additional sources of noise that arise at the pixel level. The proposed approach exploits the adaptive fitting of a logistic function to compute correcting coefficients that harmonize the two spectral sets. This short Letter addresses usage conditions and compares results against the existing state of the art.

https://doi.org/10.1364/OL.478691

In recent years, many fields of research have experienced the deployment of reflectance imaging spectroscopy (RIS), also commonly known as hyperspectral imaging, often simultaneously combining the performances of imagers in the visible (VIS), near-infrared (NIR), and short-wave-infrared (SWIR) regions of the electromagnetic spectrum [1–5]. Albeit two different spectral sensors may capture the same physical quantity, namely spectral radiance, the reported values will hardly match if compared at corresponding wavelengths. The difference in response, which, on visual observation of two complementary spectra, results in what has been defined in the literature as a "radiometric jump," "stepped data," or "spectral discontinuity," arises from a variety of factors that have been extensively studied by manufacturers in the field of spectroscopy [6,7]. Hemmer and Westphal [8] identified that a detector responsible for the observation of visible light was largely affected by warm-up time, causing spectral sensitivity drift. Hueni and Bialek [7] modeled the behavior of a visible–near-infrared (VNIR) sensor as a function of ambient temperature, while they found that the response of the infrared detector was not affected. One of the main reasons for the presence of discontinuities is the decreasing signal-to-noise ratio (SNR) at the extremities of the sensitive regions of the semiconductor materials from which the detectors are built: indeed, the absorption coefficients of the most commonly used semiconductors rarely overlap [9], making it hard to obtain a reliable combination of sensors in a wide range of wavelengths. For example, silicon (Si), the most used material to detect visible radiation, ends its operational range at around 1000 nm [10]. Such materials as indium-gallium-arsenide (InGaAs) and mercury-cadmium-telluride (HgCdTe) are used to detect infrared radiation, but need to be accurately designed (with an intrinsic concentration of elements) and appropriately cooled to be able to sense radiation at about 1000 nm [11]. Another factor that possibly generates jumps is the switch in bandwidth between two adjacent sensors, which leads to a different amount of energy incoming on the detectors, even for the same nominal wavelength.

Solutions to the problem of radiometric jumps are often referred to in the spectroscopy literature as "splicing correction" and include additive, multiplicative [12], and parabolic [13] correction routines. While the former two make use of a global correction scalar or coefficient, the latter solution proposes a wavelength-dependent coefficient to erase the radiometric jump by matching one spectrum to the other. Hueni and Bialek [7] state that multiplicative and additive corrections lead to the introduction of more errors in the spectra, especially when considering high-energy spectra, while the parabolic method efficiently matches jumps up to a 6% difference, but struggles to correct larger spectral discrepancies.

In VNIR–SWIR RIS, although observed [14], the problem has not been deeply studied by the research community. In remote sensing and airborne applications, the bands around 970 nm are sometimes not processed, owing to the presence of a water absorption band [15], while with the motivation of low SNR, it is commonly accepted for laboratory applications to discard such flawed spectral bands and conduct further steps of analysis on disconnected or independent image datasets [1]. However, there is a need to preserve as much as possible of the available information to enhance visualization methods and to be able to highlight important spectral signatures in the interval of wavelengths that could be lost. When an imaging application is considered against a spectroscopy one, it is necessary to extend the list of factors that generate spectral discrepancies at the pixel level. First of all, the magnitude of the jumps is highly influenced by the performances of image registration, especially in the case in which the two images have different (x, y) dimensions and a scale difference exists. In this case, despite the fact that sub-pixel accuracy can be achieved, the perfect pixel correspondence is an ideal condition. Moreover, reproducing the exact same relative positioning of object–illumination–camera is a rather difficult task when two separate imagers are deployed in an environment that can be adjusted only manually, and spurious differences in

Table 1. Technical Specifications of VNIR1800 and SWIR384 Hyperspectral Imagers

Name	VNIR	SWIR
Sensor	Si (CMOS)	HgCdTe
Cooling	NA	150 K
Spatial lines	1800	384
Spectral range [nm]	400–1000	1000–2500
FWHM [nm]	3.26	5.45

bidirectional reflectance distribution function (BRDF) [16] at the pixel level may generate a small difference in response.

Okyay and Khan [17] adapt the parabolic correction (PAR) routine to concatenate VNIR and SWIR hyperspectral images of airborne sensing. In our previous attempt [18], global coefficients were learned through the optimization of a joint radiometric correction performed on standardized targets, but the results could not correctly generalize in terms of spectral variability and jump magnitude.

We propose a new adaptive splicing correction routine for complementary hyperspectral images that share an overlap of nominal wavelengths. Furthermore, we propose an evaluation that compares the results obtained with the proposed solution against the state of the art represented by the parabolic splicing correction. In this specific case, we consider a laboratory use of dual RIS in the VNIR and SWIR regions, deploying push-broom hyperspectral imagers manufactured by Hyspex (NEO, Norway), for which the main specifications are reported in Table 1. On inspection of the data, it is noticeable that the spectral ranges overlap in the region between 950 nm and 1000 nm, with 16 and 9 bands for VNIR and SWIR, respectively. The pre-processing of the images includes radiometric calibration and co-registration, adopting the methodology proposed by Conover *et al.* [19] and following the guidelines highlighted in one of our previous studies [20].

The laboratory conditions of the setup accentuate possible differences in BRDF, owing to the manual positioning of the illumination sources and the hyperspectral imagers. Thus, the experimental setup (schematically reported in Fig. 1) must be designed in a way that respects, as much as possible, the same illumination geometry for the two imagers. This also implies that the cameras are carefully aligned, both to maximize the overlap of the fields of view and to reduce pixel-wise differences of the BRDF. Furthermore, it will be necessary to calibrate the scene radiance captured by the two cameras and move into an illumination-independent space (absolute spectral reflectance),

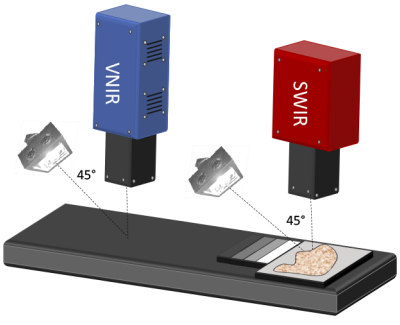

Fig. 1. Acquisition setup of simultaneous push-broom VNIR–SWIR RIS. The illumination geometry (45/0) is carefully adjusted for both imagers; however, differences in SPD of the individual light source may exist.

as there might be differences in the spectral power distribution (SPD) of the deployed illumination sources as well.

Let $\mathbf{F}(x, y, \lambda)$ be a spectral image defined in the image domain $\mathcal{D}$ with spatial coordinates (x, y) and spectral sampling in correspondence of wavelengths $\lambda \in \Lambda$. Generally, Λ is defined in $[\lambda_{\min}, \lambda_{\max}]$, but in our specific case it is the result of two separate image capture processes that generate $\mathbf{V}(x, y, \lambda_v)$ with $\lambda_v \in \Lambda_v$, $\Lambda_v = [400, 1000]$ nm and $\mathbf{S}(x, y, \lambda_s)$ with $\lambda_s \in \Lambda_s$, $\Lambda_s = [1000, 2500]$ nm. Therefore, there exists a shared interval of wavelengths $\Lambda' = \Lambda_v \cap \Lambda_s$. Assuming that $\mathbf{V}$ and $\mathbf{S}$ are spatially co-registered and equally sampled in Λ', we can define $\mathbf{V}'(\lambda')$ and $\mathbf{S}'(\lambda')$. We aim to find the transform $\mathcal{T}$ that associates (dropping the spatial coordinates for readability):

$$\mathbf{F}(\lambda) = \mathcal{T}(\mathbf{V}(\lambda_v), \mathbf{S}(\lambda_s)). \tag{1}$$

For each image it is also possible to define the set of bands that lie outside of the overlapping range as $\Lambda_v'' = \Lambda_v \setminus \Lambda'$ and $\Lambda_s'' = \Lambda_s \setminus \Lambda'$, associated to the *truncated* spectral images $\mathbf{V}''(\lambda_v'')$ and $\mathbf{S}''(\lambda_s'')$.

The region in which $\mathbf{V}'$ and $\mathbf{S}'$ lie is where the radiometric jumps take place. Because of the aforementioned noise sources (different bandwidth, decreasing SNR, differences in BRDF, and sub-pixel misregistration), we assume that neither of the overlapping sets is a reliable estimate of the final spectrum. For this reason, we decide that a possible correct position could be the mean between $\mathbf{V}'$ and $\mathbf{S}'$, noticing that this observation can be adjusted based on specific priors:

$$\mathbf{R} = \frac{1}{2}(\mathbf{V}' + \mathbf{S}'). \tag{2}$$

Then we can define correcting coefficients Φ_v' and Φ_s' for VNIR and SWIR, valid in the overlapping region, such as

$$\mathbf{R} = \Phi_v'\mathbf{V}' = \Phi_s'\mathbf{S}'. \tag{3}$$

When using the mean value as a reference for matching, the correcting coefficients will be found symmetrically distributed around 1. Ideally, the spliced spectrum should preserve the shapes of the original spectra and also match their magnitude values at some points away from the overlapping range. To do so, the correcting coefficients should smoothly vary from the values of Φ_v' and Φ_s' to 1. We achieve this by deploying a logistic function. In such a distribution, three parameters must be defined: the maximum value L, the slope k, and the center of the distribution x_0.

In this specific case, L is either the unity value or the coefficient at the extreme of the overlapping range: $\varphi_v \in \Phi_v'$ (first coefficient) and $\varphi_s \in \Phi_s'$ (last coefficient), while k and x_0 are determined as a function of the distance Δr between $\mathbf{V}'$ and $\mathbf{S}'$:

$$\Delta r = \sqrt{\frac{1}{N'}\sum_{i=1}^{N'}(\mathbf{V}' - \mathbf{S}')^2}, \tag{4}$$

in which N' is the number of bands in the overlapping range. In typical VNIR–SWIR applications, the values of Δr follow the probability density function depicted in Fig. 2. Here, we can observe that a value of 6% can already be considered very large.

The center of the logistic curve x_0 is intrinsically linked to the width of the spectral window that will experience the correction, as it is the median value of the selected interval. Therefore, λ_0 is obtained indirectly from the modeling of the window width w. To obtain smoothly connected spectra, it is desirable to have a

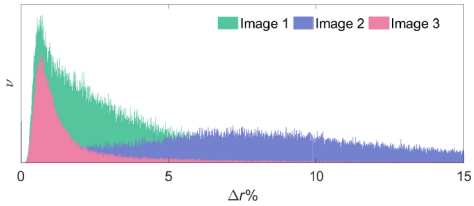

Fig. 2. Typical relative spectral discrepancy histograms stemming from three hyperspectral images.

steeper slope (higher k) and a low w (number of spectral bands affected by the correction) when the value of Δr is small, and vice versa. The window width w is modeled as a logistic function of the form:

$$w_v = \frac{N_v''}{1 + \exp\left[-c_v\left(\Delta r - x_{0v}\right)\right]}, \qquad w_s = \frac{N_s''}{1 + \exp\left[-c_s\left(\Delta r - x_{0s}\right)\right]}, \tag{5}$$

in which N_v'' and N_s'' represent the number of bands in Λ_v'' and Λ_s'', respectively. The parameters c_v, c_s, x_{0v}, and x_{0s} are learned by fitting the logistic function to the logarithmically spaced values of Δr, in an interval that can be case-specific (in the case of correction of a pair of spectra) or empirically learned from the Δr distribution (in the case of images and large spectral libraries). We can now define $\Lambda_v''' \subset \Lambda_v''$ and $\Lambda_s''' \subset \Lambda_s''$ as the subsets that experience the splicing correction with a number of bands equal to w_v and w_s, respectively. The central wavelengths λ_{0v} and λ_{0s} are then the median values of such intervals.

The slope k_v of the VNIR range can be found as the exponential function:

$$k_v = a \cdot \exp\left(b\Delta r\right) + y, \tag{6}$$

in which the parameters a, b, and y are retrieved by fitting the function to a linear vector decreasing from 1 to 0. We note here that if the modeling is performed in the same way for the SWIR counterpart, the normalization in [0,1] brings the fits of k_v and k_s to match. However, we can use prior information to model k_s so that it generates a flatter logistic curve, since the affected wavelength interval is larger:

$$k_s = k_v \frac{N_v''}{N_s''}. \tag{7}$$

The correction coefficients in Λ_v'' and Λ_s'' can now be determined as

$$\psi_v(\lambda_v'') = \frac{\operatorname{sgn}(\varphi_v - \varphi_s)}{1 + \exp\left[-k_v\left(\lambda_v'' - \lambda_{0v}\right)\right]}|\varphi_v - 1| + 1, \qquad \psi_s(\lambda_s'') = \frac{\operatorname{sgn}(\varphi_v - \varphi_s)}{1 + \exp\left[-k_s\left(\lambda_s'' - \lambda_{0s}\right)\right]}|\varphi_s - 1| + \varphi_s. \tag{8}$$

The full, smoothly connected hyperspectral image is obtained by concatenating along the spectral dimension (dropping the λ-dependency for readability):

$$\mathbf{F} = \left[\mathbf{V}'' \cdot \Psi_v,\ \mathbf{R},\ \mathbf{S}'' \cdot \Psi_s\right]. \tag{9}$$

An example of splicing correction on measured spectra can be found in Fig. S1 in Supplement 1.

The problem of spectral splicing has an infinite number of solutions, as two spectra can be connected and modified in infinite ways, but only a limited set of pertinent solutions. Thus, the evaluation of the final spectrum and the validation of the methodology can be tricky. To help the evaluation, a Lambda1050 spectroradiometer (Perkin Elmer inc.) was deployed to obtain a continuous ground truth measurement in the interval 400–2500 nm. Such an instrument deploys two sensors: a photomultiplier tube (PMT) for the range 400–860 nm and an indium-gallium-arsenide (InGaAS) detector for the range 861–2500 nm. Therefore, the spectral region of interest of the VNIR–SWIR splicing correction is included in a single sensor (InGaAs) sensitivity range. A total of 175 samples coming from a collection of oil-painted mockups [21] were measured. Such samples possess a level of texture high enough to produce slight differences in BRDF at the pixel level. In evaluating the final result, two properties of the reconstructed spectra were evaluated:

(1) Conformity with the spectral shape of the ground truth, evaluated through the usage of spectral angle (SA) [22];
(2) Minimum intervention on the original spectra, measured by means of the root mean square percentage error (RMSPE) [23].

The rationale behind the choice of not considering a metric that compares the absolute reflectance values of the ground truth and the VNIR–SWIR spectra resides in the fact that the spectroradiometer averages the measurement over an area, while the highly textural samples possess a high degree of spectral variability that makes the magnitude comparison meaningless at the pixel level. Furthermore, the acquisition geometries of hyperspectral capture and spectroscopy are different.

The proposed method [logistic correction (LOG)] is compared against the existing state of the art of splicing correction in spectroscopy. The PAR method was adapted following the insight of Okyay and Khan [17] and correcting the last 60 bands of the VNIR. The first VNIR wavelength to be corrected is then 785 nm, while the juncture point was selected in the middle of the overlap area at 973 nm. Although discouraged from usage, we also include the multiplicative correction (MUL) method, computing the global coefficient as the ratio between the SWIR and VNIR bands at 950 nm.

Since the selected correction methods affect a different number of bands, it is necessary to compare the evaluation metrics in turn in the relative intervals of influence, as reported on the x axis of Fig. 3. The results of SA between the spliced spectra and the ground truth are, however, affected by the SA that exists between

Fig. 3. Mean values for (a) RMSPE, (b) SA, and (c) ΔSA in different intervals of affected spectral bands: LOG, logistic correction; PAR, parabolic correction; and MUL multiplicative correction.

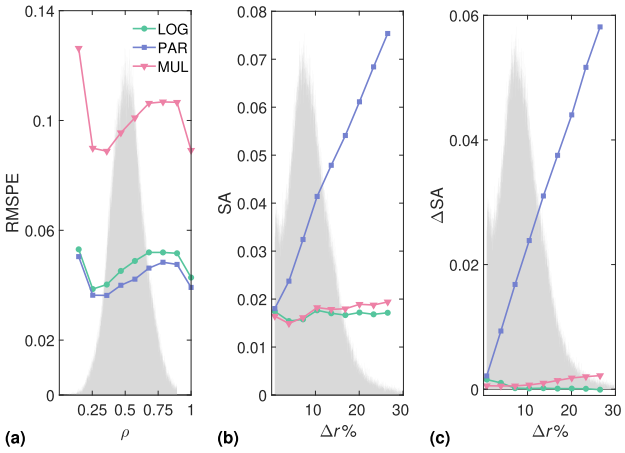

Fig. 4. Behavior of selected correction methods in specific cases of (a) spectral energy and (b), (c) spectral discrepancy. The overlaid histograms (normalized for display purposes) illustrate the probability distributions of the events of spectral energy ρ and relative spectral discrepancy $\Delta r\%$.

the original disconnected spectra and the ground truth. For this reason, it was decided to analyze the difference of SA (ΔSA), as shown in Fig. 3(c). Figure 3(a) highlights how the MUL method introduces a lot of unnecessary perturbations, while the PAR and LOG methods achieve fairly similar results. From Figs. 3(b) and 3(c) it is possible to notice that the proposed LOG method produces more faithful spectral shapes consistently.

Figure 4 highlights the limitations of the MUL and PAR methods in some specific cases. When considering a global coefficient for the whole spectrum, the relative magnitude perturbation that is introduced is highly impacting when the energy of the spectrum is low, as Fig. 4(a) depicts. Conversely, the PAR method shows a rapidly increasing perturbation in spectral shape as the spectral discrepancy also increases [Figs. 4(b) and 4(c)], confirming the previous observation of Hueni and Bialek [7]. The proposed LOG method is proved to be more stable to such specific cases that have, anyway, a likely occurrence, as depicted by the frequency histograms of spectral energy at the overlap and relative spectral discrepancy.

In summary, we propose a new adaptive splicing correction routine to smoothly connect hyperspectral images that present spectral jumps in correspondence of adjacent spectral sensitivity intervals. The correction is performed in absolute reflectance space and it is adaptive in the sense that the amount of spectral bands affected depends on the magnitude of the initial spectral discrepancy. Advantages against the existing state of the art include better stability in cases of larger spectral discrepancies, which are more likely to occur in the case of imaging than in point spectroscopy. The proposed method presents, however, a few shortcomings in splicing specific spectral shapes, as we highlight in Figures S2 and S3 in Supplement 1. Therefore, it will be necessary in the future to extend the modeling of splicing correction to account for different levels of spectral complexity.

Disclosures. The authors declare no conflicts of interest.

Data availability. Data underlying the results presented in this paper are available in Ref. [24]

Supplemental document. See Supplement 1 for supporting content.

REFERENCES

1. J. Sandak, A. Sandak, L. Legan, K. Retko, M. Kavčič, J. Kosel, F. Poohphajai, R. H. Diaz, V. Ponnuchamy, N. Sajinčič, O. Gordobil, C. Tavzes, and P. Ropret, Coatings **11**, 244 (2021).
2. A. Siedliska, P. Baranowski, M. Zubik, W. Mazurek, and B. Sosnowska, Postharvest Biol. Technol. **139**, 115 (2018).
3. C. Camino, V. González-Dugo, P. Hernández, J. Sillero, and P. J. Zarco-Tejada, Int. J. Appl. Earth Obs. Geoinf. **70**, 105 (2018).
4. M. Selva, B. Aiazzi, F. Butera, L. Chiarantini, and S. Baronti, IEEE J. Sel. Top. Appl. Earth Observations Remote Sensing **8**, 3008 (2015).
5. J. K. Delaney, J. G. Zeibel, M. Thoury, R. Littleton, M. Palmer, K. M. Morales, E. R. de La Rie, and A. Hoenigswald, Appl. Spectrosc. **64**, 584 (2010).
6. M. Danner, M. Locherer, T. Hank, and K. Richter, GFZ Data Services, (2015).
7. A. Hueni and A. Bialek, IEEE J. Sel. Top. Appl. Earth Observations Remote Sensing **10**, 1542 (2017).
8. T. H. Hemmer and T. L. Westphal, Algorithms for Multispectral, Hyperspectral, and Ultraspectral Imagery VI **4049**, 249 (2000).
9. D. Benedikovic, L. Virot, G. Aubin, J.-M. Hartmann, F. Amar, X. Le Roux, C. Alonso-Ramos, É. Cassan, D. Marris-Morini, J.-M. Fédéli, F. Boeuf, B. Szelag, and L. Vivien, Nanophotonics **10**, 1059 (2021).
10. B. Jalali and S. Fathpour, J. Lightwave Technol. **24**, 4600 (2006).
11. G. L. Hansen, J. Schmit, and T. Casselman, J. Appl. Phys. **53**, 7099 (1982).
12. W. Dorigo, M. Bachmann, and W. Heldens, *User's Manual, German Aerospace Center (DLR), Oberpfaffenhofen* (German Aerospace. Centre, 2006).
13. D. Beal and M. Eamon, *Analytical Spectral Devices, Inc.* (2009).
14. R. J. Murphy, S. T. Monteiro, and S. Schneider, IEEE Trans. Geosci. Remote Sensing **50**, 3066 (2012).
15. J. A. Curcio and C. C. Petty, J. Opt. Soc. Am. **41**, 302 (1951).
16. F. O. Bartell, E. L. Dereniak, and W. L. Wolfe, Radiation scattering in optical systems **0257**, 154 (1981).
17. U. Okyay and S. D. Khan, Photogramm. Eng. Remote Sensing **84**, 781 (2018).
18. F. Grillini, J.-B. Thomas, and S. George, Color and Imaging Conference **29**, 276 (2021).
19. D. M. Conover, J. K. Delaney, and M. H. Loew, Appl. Phys. A **119**, 1567 (2015).
20. F. Grillini, J.-B. Thomas, and S. George, *2022 12th Workshop on Hyperspectral Imaging and Signal Processing: Evolution in Remote Sensing (WHISPERS)* (2022), pp. 1–5.
21. F. Grillini, J.-B. Thomas, and S. George, Sensors **21**, 2471 (2021).
22. F. A. Kruse, A. Lefkoff, J. Boardman, K. Heidebrecht, A. Shapiro, P. Barloon, and A. Goetz, Remote Sens. Environ. **44**, 145 (1993).
23. H.-S. Lee and M.-T. Chou, Int. J. Comput. Math. **81**, 781 (2004).
24. F. Grillini, "Hyperspectral Splicing Correction," Github (2019), [accessed 19 October 2022], https://github.com/federigr/HyperspectralSplicingCorrection.